Desalination and Water Treatment
www.deswater.com

doi: 10.5004/dwt.2017.21451

95 (2017) 128–143
November

Hybridizing carbon nanomaterial with powder activated carbon for an efficient removal of Bisphenol A from water: the optimum growth and adsorption conditions

Haiyam Mohammed Alayan[a,b], Mohammed Abdulhakim Alsaadi[a,c,d,*], Ali Abo-Hamad[a,b], Mohamed Khalid AlOmar[a,e], Mustafa Mohammed Aljumaily[a,c], Rasel Das[f], Mohd Ali Hashim[a,b]

[a]*University of Malaya Centre for Ionic Liquids, University Malaya, 50603 Kuala Lumpur, Malaysia, Tel. +60163630693; Fax: +60 3 7967 5311; email: mdsd68j@gmail.com (M.A. Alsaadi), Tel. +601121881804; email: hayomchm@yahoo.com (H.M. Alayan), Tel. +46 739138360; email: aliabohamad@yahoo.com (A. Abo-Hamad), Tel. +60182238504; email: mohd.alomar@yahoo.com (M.K. AlOmar), Tel. +60188716877; email: mustafa.kh1989@gmail.com (M.M. Aljumaily), Tel. +60176706452; email: alihashim@um.edu.my (M.A. Hashim)*
[b]*Department of Chemical Engineering, University of Malaya, 50603 Kuala Lumpur, Malaysia*
[c]*Nanotechnology and Catalysis Research Centre (NANOCAT), University of Malaya, 50603 Kuala Lumpur, Malaysia*
[d]*National Chair of Materials Science and Metallurgy, University of Nizwa, Sultanate of Oman*
[e]*Department of Civil Engineering, University of Malaya, 50603 Kuala Lumpur, Malaysia*
[f]*Chemical Department, Functional Nano & Micro-Structured Surface, Leibniz-Institute for Surface Modification, Permoserstr. 15, D-04318 Leipzig, Germany, Tel. +49 (0)341 235 Ext. 3147; email: raselgeneticist@gmail.com*

Received 30 March 2017; Accepted 19 September 2017

ABSTRACT

This work focuses on the optimization of experimental factors affecting the adsorptive removal of Bisphenol A (BPA) using a response surface methodology in combination with central composite design. Thus, a multistructure carbon nanomaterial hybrid was prepared using chemical vapor deposition of methane onto powder activated carbon loaded with nickel nanoparticles. The effects of various growth parameters, including growth temperature, reaction time, and gas ratio were assessed and correlated with quantitative responses. The highest yield of hybrid nanomaterial and removal percentage of BPA were found at growth temperature, reaction duration, and feed gases ratio (H_2/CH_4) of 950°C, 20 min, and 1.0, respectively. Optimization for adsorption conditions namely pH, adsorbent dose, and contact time was performed using the selected carbon nanomaterial hybrid sample. The adsorption kinetics followed accurately the pseudo-second-order model. Langmuir isotherm model provides an excellent model with a maximum adsorption capacity of 181.8 mg g^{-1}.

Keywords: Carbon nanomaterials synthesis; Adsorption; Response surface methodology; Bisphenol A; Chemical vapor deposition

1. Introduction

Bisphenol A (BPA) is a phenolic endocrine disrupting chemical commonly used in the production of polycarbonate plastics, epoxy resins, and polysulfones. However, BPA leaches easily into aqueous phases and affects the estrogenic activity in consumers. Moreover, BPA can cause neurological disorders, diabetes, and cardiovascular disease. Due to the serious health risks of releasing BPA, efforts should be made to remove the BPA from the aquatic environment [1]. Water remediation using adsorption techniques has been

---

* Corresponding author.

considered as a key approach for the removal of organic contaminants. Compared with other water treatment methods, adsorption offers an effective and economical solution because of the high efficiency, design simplicity, operational reliability, and the ability to recover adsorbents [2].

The unique properties of carbon nanomaterials (CNMs), including their shape, surface area, electronic, thermal, and sorption properties, have made them highly useful for environmental applications [3]. Generally, several synthetic schemes were used to produce CNMs, including arc discharge, laser ablation, and chemical vapor deposition (CVD) [4]. Nevertheless, the versatility CVD approach has made it favorable since it represents a cost-effective technique and provides products with high purities under controlled growth conditions [5,6].

Porous materials, including silica gel and zeolites, are excellent catalyst supports that have been frequently used for carbon nanotubes (CNTs) production [7–9]. Activated carbon materials are well-established in the field of adsorption applications due to their exceptional removal ability and effective recollection after use by conventional separation processes [10]. In addition, the growth of CNMs on activated carbon substrate is boosted due to the abundant porous structure of activated carbon, and its applicability to hold metallic catalyst particles [11,12].

The pyrolysis of hydrocarbon gases in the CVD method usually requires fine metal catalyst seeds of elements such as Ni, Fe, or Co to start nanostructure growth [13–15]. These metals have a high binding energy with carbon, leading the carbon-containing gases to form reactive species through a dissociative chemisorption process [2,16,17]. Powder activated carbon (PAC) assists the catalytic production of CNMs through dispersing well the catalyst particles and preventing the coalescence at high temperatures [18]. AlSaadi et al. [19] reported that PAC could catalyze effectively CNMs growth and improves the sorption capacity of heavy metals from aqueous solutions. Overall, the structure of deposited CNMs depends basically on the working conditions, including temperature, growth duration, carbon source, feed gas flow rate, and the presence of carrier gas [20].

Carbon nanomaterial hybrid (CNMH) can form multidirectional/multistructure integrated networks with unique physical, electronic, and chemical properties. In such hybrids, the exciting characteristics of CNMs coupled with the large porous structure and rapid adsorption capability of activated carbon [21].

The removal of BPA by adsorption has been widely explored by many researchers using various adsorbents. Zheng et al. [22] reported that the maximum adsorption capacity of BPA using organoclays was 151.52 mg g^{-1}. Tsai et al. [8] showed that the hydrophobic zeolite has excellent affinity for BPA removal from aqueous solution. In another study, the commercial and synthesized chitosan revealed a maximum adsorbent uptake for BPA of 27.02 and 34.48, respectively [23]. Xu et al. [24] reported that the maximum adsorption capacity obtained from Langmuir isotherm for BPA decontamination using graphene was 182 mg g^{-1}. According to Dehghani et al. [23] investigation, the maximum adsorption capacities of BPA by single-walled carbon nanotubes (SWCNTs) and multi-walled carbon nanotubes (MWCNTs) were 71 and 111 mg g^{-1}, respectively.

There are few examples for the application of nanocarbon/carbon hybrids in water treatment and purification [25–27]. Herein, CNMH was prepared on low-cost PAC impregnated with a Ni catalyst using CVD method. The hydrothermal growth parameters, including reaction temperature, growth duration, and ratio of feed reaction gases (methane and hydrogen), were optimized. The novel carbon nanohybrid adsorbent was characterized using field-emission scanning electron microscopy (FESEM), transmission electron microscopy (TEM), energy-dispersive X-ray spectroscopy (EDX), Raman spectroscopy, Fourier transform infrared spectroscopy (FTIR), thermogravimetric analysis (TGA), Brunauer–Emmett–Teller (BET), and zeta potential. In the second stage, further optimization of the removal parameters, including pH, CNMH dosage, and contact time, was carried out for BPA adsorption. Response surface methodology (RSM) accompanied by analysis of variance (ANOVA) were applied to describe the possible interactions between process variables and then select the significant model [28,29].

2. Experiments and methodology

2.1. Chemicals and gases

All chemicals were supplied by Sigma-Aldrich (Malaysia) as analytical grade and used without further purification. A coal-based commercial PAC was used as a substrate material in this work. Acetone was used as a solvent for catalyst impregnation, and nickel(II) nitrate ($Ni(NO_3)_2{\cdot}6H_2O$) (purity > 95%) as source of nickel (Ni^{2+}) ions catalyst. BPA (purity 99%) ($(CH_3)_2C(C_6H_4OH)_2$) for contaminated water preparation. Hydrochloric acid (36.5%–38%) and sodium hydroxide pellets for pH adjustment. Gases used for production of CNMs were: methane (CH_4), purified hydrogen (H_2), and purified nitrogen (N_2). All gases were provided by MOX® Gases Berhad, Malaysia, with 99.99% purity grade.

2.2. Preparation of the CNMH

2.2.1. Catalyst impregnation

Nickel(II) nitrate ($Ni(NO_3)_2.6H_2O$) was introduced as the catalyst precursor and impregnated into the support pores of PAC. Before running the growth experiment, PAC was dried overnight at 120°C. A solution of 1% w/v nickel(II) nitrate was prepared in acetone and mixed with 2.0 g of PAC. The mixture was sonicated for 1 h at 60°C and then heated in the oven at 120°C overnight to complete dryness. Later, metal catalyst nanoparticles were prepared using, thermal treatment of two stages including a calcination process at 550°C for 2 h in N_2 atmosphere, followed by a reduction using H_2 gas at 350°C for 1 h using the CVD tubular furnace. The final impregnated substrate (Ni-PAC) was then used for CNMH growth [30].

2.2.2. Optimization of CNMH growth

A design of experiment (DOE) with a central composite design (CCD) was employed to optimize the synthesis parameters, including hydrothermal temperature, growth time, and hydrogen to hydrocarbon source flow rate ratio (H_2/CH_4) [31]. In this study, the percentage of carbon nanomaterial hybrid yield (CNMHY) and BPA removal efficiency (RV1%) were selected as process responses and the results were represented in the form of a tridimensional graph at optimal conditions. Table 1 shows the growth variables studied for CH_4 decomposition, denoted as *A*, *B*, and *C*, and represented at coded levels of –1, 0, and +1. A set of 14 growth experimental runs were conducted to be applied in the response surface analysis.

Growth processes were executed using the CVD method inside a dual zone tube electrical furnace. In total, 200 mg of the thermally treated Ni-PAC was placed in the middle of the tubular reactor. CH_4 was used for the synthesis under a temperature range of 750°C–1,000°C and introduced with a volumetric flow ratio H_2:CH_4 ranging from 1 to 5. To initiate the growth, the flow of the carbon source was allowed to pass through the heated reactor for periods between 20 and 60 min. Finally, the reactor was cooled to room temperature under a pure N_2 stream [32]. The first response (CNMHY) was calculated by measuring the weight difference between CNMH after the growth and the PAC substrate that holds only the catalyst particles, following the formula:

$$\text{Yield } \% = \frac{m_{\text{after}}^{\text{catal}} - m_{\text{blank}}^{\text{catal}}}{m_{\text{blank}}^{\text{catal}}} \times 100\% \qquad (1)$$

where $m_{\text{after}}^{\text{catal}}$ is the total mass of the product after the reaction, and $m_{\text{blank}}^{\text{catal}}$ is the weight of the PAC substrate treated similarly to growth reaction conditions, but without the introduction of any carbon sources.

To generate the second response (RV1%), batch adsorption experiments were conducted on the carbonaceous material produced from each of the 14 growth experimental runs. A fixed dosage of each adsorbent (10 mg) was placed into 50 mL Erlenmeyer flask of BPA (50 mg L^{-1}) and shaken for 120 min at a constant agitation speed (180 rpm) at room temperature. In addition, pH of the solution in all tests was maintained at pH = 6.0. A known volume of the solution was removed at the end of the adsorption time and centrifuged at 4,000 rpm for 10 min. The BPA concentration in the supernatant was measured by UV–Vis spectrophotometry through monitoring the maximum absorbance wavelength at 277 nm [33]. The BPA removal efficiency percentage (RV1%) was calculated using Eq. (2):

$$\text{Removal efficiency } \% = \frac{C_0 - C_t}{C_0} \times 100 \qquad (2)$$

where C_0 and C_t (mg L^{-1}) are the liquid-phase concentrations at the initial time point and after 120 min, respectively. Subsequently, RSM analysis was applied to optimize growth variables in order to predict the best value for responses. A list of design experiments runs and the ANOVA of both responses for CNMH are presented in Tables S1–S3 (supplementary material).

2.2.3. Adsorption of BPA onto CNMH adsorbent

The second set of experiments demonstrates the optimization of BPA removal by CNMH obtained at the optimal conditions. The DOE analysis required 15 experimental runs (shown in supplementary material), and the investigated parameters are denoted as x_1 for the pH, x_2 for the CNMH dosage (mg), and x_3 for the time (min). Coded levels and adsorption parameters are provided in Table 2. Two responses in the adsorption process were considered: BPA removal efficiency percentage (RV2%) and adsorption capacity (*Q*, mg g^{-1}). The 3-D graphical responses of the studied parameters were used to describe the parameters influencing the process and resulting interactions.

The adsorption experiments were performed in the same manner as described in the previous section under varying conditions for pH (2–12), adsorbent dose (5–15 mg), and contact time (20–120 min) with an initial BPA concentration of 50 mg L^{-1}. The stock solution was prepared by dissolving 50 mg of BPA in a 1,000 mL volumetric flask followed by dilution up to the mark by addition of deionized water. The removal efficiency (%) was determined according to Eq. (2) and the equilibrium adsorption uptake, Q_e (mg g^{-1}), was calculated using the following equation:

$$\text{Adsorbent uptake, } Q_e = \frac{C_0 - C_e}{w} \times V \qquad (3)$$

where C_0 and C_e (mg L^{-1}) are the liquid-phase concentrations at initial and equilibrium states, respectively. *V* (L) is the volume of BPA solution and *w* (g) is the adsorbent dosage.

2.2.4. Kinetic studies

A convenient expression of the reaction mechanism rate was provided by kinetic modeling. The kinetic models summarized in Table 3, including pseudo-first-order, pseudo-second-order, and intraparticle diffusion, were applied in order to correlate the experimental data of obtained CNMH. Kinetics studies were performed using a series of adsorption experiments at regular time intervals (5, 10, 20, 25, 30, 40, 50, 60, 70, 80, 100, 110, 120, 130, 140, 150, 160,

Table 1
Experimental range and levels of the independent variables for CNMH synthesis

Independent parameters	Range (coded levels)	
	Low (–1)	High (+1)
Temperature (*A*), °C	750	1,000
Growth time (*B*), min	20	60
H_2/CH_4 flow rate	1	4

Table 2
Experimental design for batch adsorption of BPA using CCD

Independent parameters	Range (coded levels)	
	Low (–1)	High (+1)
pH (x_1)	2	12
CNMH dosage (x_2), mg	5	15
Time (x_3), min	20	120

170 min, and 24 h), whereas other conditions were chosen based on the second set of optimization results suggested by the DOE.

2.2.5. Adsorption isotherms

BPA adsorption characteristics can be expressed in terms of isotherm diagrams, including Langmuir, Freundlich, and Temkin. The investigated models and their outcome parameters are presented in Table 4.

A stock solution of BPA was prepared at a concentration of 100 mg L^{-1}. For the adsorption isotherm experiments, lower concentrations were produced (i.e., 5, 10, 20, 30, 40, 50, 60, 70, 80, and 90 mg L^{-1}) by diluting with deionized water. BPA concentrations were measured for each experiment after reaching the equilibrium, while other working conditions were kept constant at the optimal values which were previously determined.

2.3. Equipment and measurements

The growth process using the CVD method was carried out in situ with an OTF-1200-80mm. Dual Zone Tube Furnace tubular reactor equipped for immediate use with one 50 mm diameter fused quartz tube (OD: 80 mm; ID: 72 mm; length: 1,000 mm).

An FESEM equipped with an EDX (Quanta FEG 450, EDX-OXFORD) was used to obtain high-resolution images of nano-sized structures to study the CNMH morphology and surface elements. Other morphological features were observed using a TEM. TGA was obtained using a thermal analyser (STA-6000, PerkinElmer®) in an oxygen environment at a heating rate of 10°C min^{-1}. Surface area analysis was performed using a gas sorption system (Micromeritics ASAP2020, TRISTAR II 3020 Kr) following the BET method. The prepared CNMs-PAC adsorbent was also characterized by Raman spectroscopy (Renishaw System 2000 Raman Spectrometer). The adsorbent surface chemistry before and after BPA adsorption was investigated using FTIR (PerkinElmer® FTIR spectrometer), during which the sample was ground with KBr to form pellets and a wavenumber in the range of 500–4,000 cm^{-1} was used. Furthermore, the dispersibility of the prepared hybrids in aqueous solutions was investigated by following zeta potential measurements using a Zetasizer (Malvern, UK). The concentrations of BPA were monitored using UV–Vis spectroscopy (PerkinElmer® spectrophotometer) [34].

3. Results and discussion

The experiments assessing CNMH growth were optimized to obtain the optimum growth conditions based on two responses: growth yield and BPA removal efficiency. Then the adsorbent, which was prepared at the optimal growth conditions, was used to optimize the conditions for BPA removal from aqueous solution.

Table 3
Parameters deduced from kinetic models for BPA adsorption on CNMH

Model	Plot	Parameters	Values
Pseudo-first-order $\ln(q_e - q_t) = \ln q_e - K_1 t$	$\ln(q_e - q_t)$ vs. time (t)	$K_1 = -$slope (min^{-1})	0.0161
		$q_e = e^{(\text{intercept})}$ (mg g^{-1})	27.107
		R^2	0.8247
Pseudo-second-order $\frac{t}{q_t} = \frac{1}{K_2 q_e^2} + \frac{1}{q_e} t$	$\frac{t}{q_t}$ vs. t	$q_e = 1/(\text{slope})$ (mg g^{-1})	144.928
		$K_2 = \frac{\text{Slope}^2}{\text{Intercept}}$ (g mg^{-1} min^{-1})	0.001608
		R^2	0.9992
Intraparticle diffusion $q_t = K_d t^{1/2} + c$	q_t vs. $t^{0.5}$	K_d = slope (g mg^{-1} min$^{-0.5}$)	2.4
		R^2	0.821

Table 4
Isotherm constant parameters and the coefficients calculated for the adsorption of BPA on the CNMH

Model	Equation	Plot	Parameters	Values
Langmuir	$C_e/q_e = 1/(K_L Q_m) + C_e/Q_m$	A plot of C_e/q_e vs. C_e should indicate a straight line of slope $1/Q_m$ and intercept of $1/(K_L Q_m)$	Q_m (mg g^{-1})	181.818
			K_L (L mg^{-1})	0.514
			R_L	0.0375
			R^2	0.9941
Freundlich	$\ln q_e = \ln K_F + (1/n)\ln C_e$	The values of K_F and $1/n$ were determined from the intercept and slope of linear plot of $\ln q_e$ vs. $\ln C_e$	$1/n$	0.38
			K_F (L mg^{-1})$^{1/n}$	56.48
			R^2	0.7316
Temkin	$q_e = B_1 \ln K_T + B \ln C_e$	Values of B_1 and K_T were calculated from the plot of q_e against $\ln C_e$	B	31.954
			K_T	8.667
			R^2	0.9207

3.1. ANOVA and optimization

3.1.1. CNMH growth yield and BPA removal efficiency

For CH_4 decomposition, a set of experimental designs with different ranges of production conditions was prepared. The nanostructure production conditions were optimized using a second-level CCD with one central point. Tables S2 and S3 show ANOVA analyses for the growth factors, specifically temperature (A), duration of synthesis (B), gases flow ratio (C), and their higher-order terms

The larger F values and smaller p values, the more significant is the corresponding coefficient term [35]. Regarding the optimization of CNMH synthesis, the F value resulted from ANOVA was 210.54 for CNMH growth yield, and 13.87 for BPA removal efficiency. This indicates that the model was significant and the response variations were expressed well by the proposed regression equation. Furthermore, values of 'Prob > F' less than 0.05 confirm that the model is statistically significant [36].

The final empirical model's equations constructed from the experimental parameters for CNMHY and RV1% for CH_4 decomposition are given in Eqs. (4) and (5), respectively.

$$\begin{aligned}\ln\left(\text{CNMHY}\right) = &-11.3533 + 0.030391A - 0.078949B \\ &+ 10.96588C + 5.78868\times10^{-5}AB - 0.025148AC \\ &- 1.09754\times10^{-5}BC - 1.54115\times10^{-5}A^2 + 4.59701\times10^{-4}B^2 \\ &+ 0.012797C^2 + 1.41316\times10^{-5}A^2C\end{aligned} \tag{4}$$

$$\begin{aligned}\text{RV1\%} = 76.21 &+ 24.55A - 9.17B + 6.34C - 17.10AB \\ &- 0.35AC - 10.09A^2 - 33.70A^3\end{aligned} \tag{5}$$

The coefficient of determination (R^2) of CNMH yield and BPA removal were 0.9986 and 0.9418, respectively. The high R^2 values and the low coefficient of variation (CV = 1.35% and 5.47%) suggest that the obtained model provides an excellent estimation of the response, which can be reproducible as long as these values are not greater than 10% [37]. Both responses exhibited desirable precisions of ~47 and ~12, respectively, since their values are above 4.0 [38]. The model suggested for CH_4 decomposition was found to be reliable in predicting the optimal yield of CNMH and BPA removal efficiency at the following reaction conditions: a temperature of 950°C, synthesis duration of 20 min, and a H_2 to CH_4 flow ratio of 1.0. Using this model, the growth yield and the removal efficiency were predicted to be 22.9% and 87.6%, respectively, while the experimental values obtained were 22.7% and 87.4% respectively, demonstrating excellent agreement with the model. In Fig. 1, it can be observed that there is a good relationship between the experimental and predicted values for both responses, since the data points exhibit a distribution that approaches a straight line. Moreover, the plots indicate that the proposed models were adequate in predicting the response variables for the experimental data.

3.1.2. Effects and interactions of variables on CNMHY and RV1%

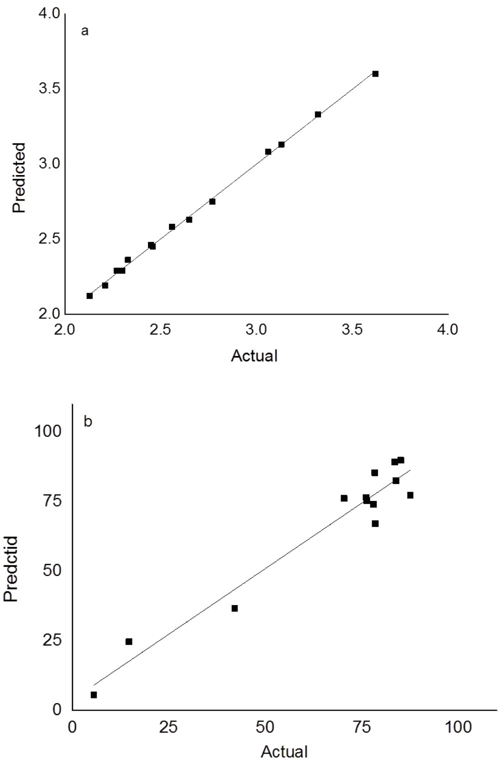

Fig. 1. Predicted vs. actual data obtained from optimizing the growth yield for (a) CNMHY and (b) RV1% using ANOVA.

Generally, if the F function is greater than 4, the product is significantly influenced by the parameter variations [39]. ANOVA results in Tables S2 and S3 show that the studied parameters significantly affect the graphitization of the prepared CNMH. Among these parameters, the reactor temperature (parameter A) and growth duration (parameter B) are the most important. The high F values for the linear terms of A and B (914.87 and 57.22, respectively) indicate that they will have a large effect on the CNMH yield. 'Prob > F' values were less than 0.01 and 0.0021 for the interaction of variables (AB) in the model, indicating their significant effect on the product yield and on BPA removal efficiency [40].

RSM results, displayed in Fig. 2(a), suggested that the yield increased proportionally with the increase in growth time, and then dropped as the reaction proceeded. However, longer reaction times were found to cause the deposition of amorphous carbon, limiting the growth duration to 20 min maximize the growth rate and minimize the formation of amorphous carbon [31]. Furthermore, Fig. 2(b) indicates that high growth temperature has more positive effects on promoting the BPA removal efficiency, compared with the impact of growth duration parameter.

3.1.3. Central composite design for BPA adsorption evaluations

Similarly, CCD was applied in the second set of experiments to evaluate the adsorption performance of the CNMH produced with the optimal production conditions. Two targeted responses were selected for the three adsorption factors: removal efficiency percentage (RV2%)

and adsorbent uptake (*Q*). The variables coded for adsorption parameters in the CCD analysis and their ranges are described in Table 2. Based on the proposed design, 15 experimental runs were performed, as summarized in Table S4. The constraints developed to control the optimization solutions of the CCD software were to maximize RV2% and *Q* by keeping adsorption variables in the ranges defined previously in Table 2. Accordingly, the optimal removal conditions were found at a pH of 3.2, adsorbent dosage of 15 mg, and removal duration of 120 min which produced the highest BPA removal efficiency (97.5%) and adsorbent uptake (181.8 mg g^{-1}). The experimental and predicted data were found close enough with R^2 correlation values of 0.9559 and 0.9941 for BPA removal efficiency and for adsorbent uptake, respectively.

ANOVA modeling for the two responses is summarized in Tables S5 and S6, which indicate that the *F* values for the models were 28.9 and 93.42 in the two optimization cases of removal efficiency and adsorbent uptake, respectively. This suggests that both models are significant and the predicted R^2 approached the adjusted values. For the removal percentage efficiency, the cases x_1 (pH), x_2 (dosage), x_3 (contact time), x_1x_2, x_2x_3 and x_2^2 offered significant model terms. However, the adsorbent capacity showed significant effects for x_1, x_2, x_3, x_1x_2, x_1x_3, x_2x_3, x_1^2, x_3^2 and $x_1^2x_3$. The adequate precision values were 19.723 and 36.048, which indicated satisfactory signals for both responses. Data analysis gave expression for RV2% and *Q* with the following equations:

$$\begin{aligned} \text{RV2\%} &= 19.1 - 2.24x_1 + 7.65x_2 + 0.202x_3 \\ &\quad + 0.00387x_1x_2 - 0.00675x_2x_3 - 0.188x_2^2 \end{aligned} \tag{6}$$

$$\begin{aligned} Q &= 287.0 - 7.81x_1 - 9.67x_2 + 4.46x_3 + 0.590x_1x_2 - 0.948x_1x_3 \\ &\quad - 0.046x_2x_3 - 0.492x_1^2 - 0.00937x_3^2 + 0.0673x_1^2x_3 \end{aligned} \tag{7}$$

Figs. 3(a) and (b) show a plot of experimental RV2% and *Q* vs. calculated values. The plots proved to be successfully reliable to represent the relation between the adsorption variables and the responses.

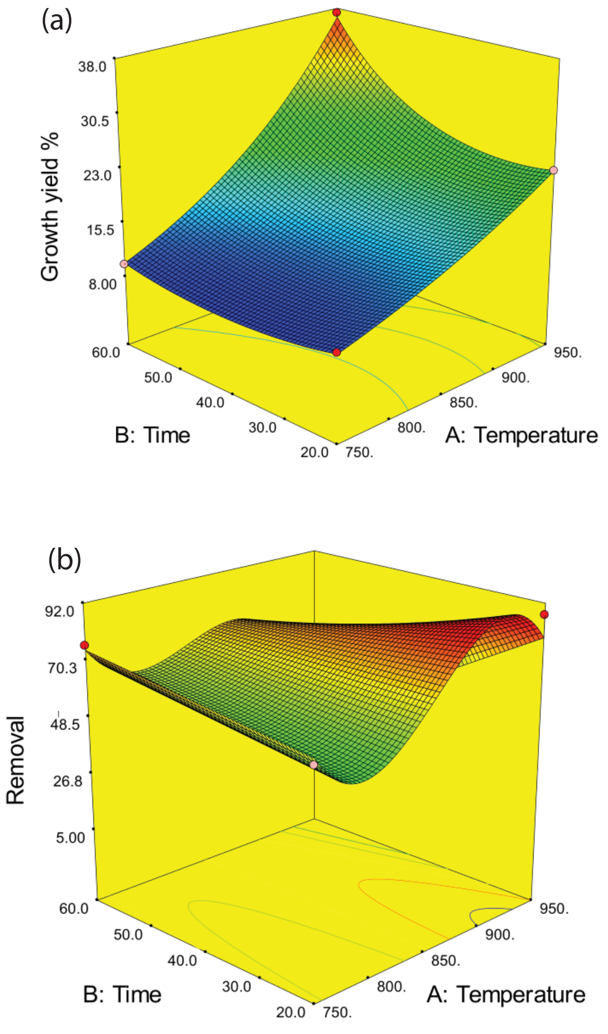

Fig. 2. RSM plots of (a) growth yield of (CNMHY) and (b) BPA removal efficiency (RV1%) considering the effect of reaction time and growth temperature.

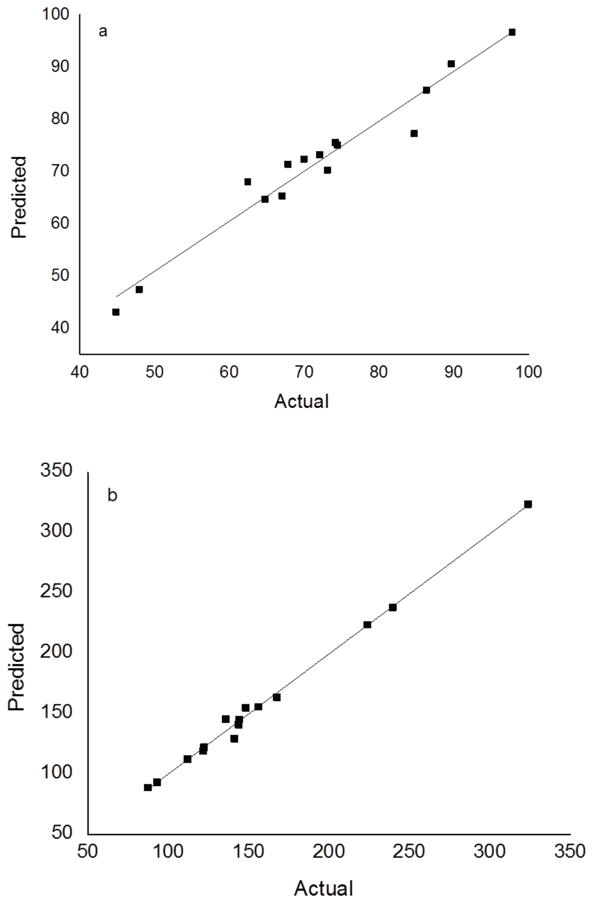

Fig. 3. Predicted vs. actual data obtained from optimizing the BPA adsorption onto CNMH for (a) removal efficiency (RV2%) and (b) adsorbent capacity (*Q*) using ANOVA.

3.1.4. Effects and interactions of individual variables on BPA adsorption

A significant effect for the linear variable terms was indicated, along with x_2^2, as shown in Table S5. The high *F* values of the adsorbent dosage parameter (79.82) confirmed the superior effects of this variable, compared with the effects of pH and contact time, which were 27.08 and 12.52, respectively. The effects of both the pH and CNMH dosage (x_1x_2) on removal efficiency were found to be more significant ($p = 0.0176$) than the combined impact of adsorbent amount and contact time (x_2x_3) ($p = 0.1343$). This can be attributed to the fact that adsorbent dosage provides a direct reflection of the surface area, while the pH corresponds to surface charge; therefore, both effects are combined in this model. The interaction effect of pH–adsorbent dosage (x_1x_2) was also valuable since it represented an *F* value of 15.44.

The adsorbent uptake showed a similar trend for the interaction between variables as in the removal efficiency of BPA (Table S6). The most significant terms that combine two factors were found for pH with adsorbent dosage ($p = 0.0055$), and for adsorbent dosage with contact time ($p = 0.0038$).

The effect of pH was found to have a remarkable influence on the efficiency of removal and the adsorption capacity, as it affects the properties of both the adsorbate and the adsorbent [41]. In this regard, the carbon surface charge and the dissociation of the electrolyte are mainly influenced by the pH. Fig. 4(a) shows the effect of pH on RV% at the optimal time. The plot indicates that the RV% increased gradually until it reached the highest value at pH 3.2. The surface charge of the adsorbent is inversely related to pH, and the H^+ competition with BPA species is reduced. Furthermore, the pK_a value of BPA is approximately 9.5, therefore, at basic pH and (especially when the pH of the solution is higher than the pK_a value of BPA), a reduction in adsorption was observed due to the growing repulsion forces and a reduction in π–π interactions between bisphenolate anions and the surface of the sorbent [42]. Results from Liu et al. [43] indicated that of the lowest amount BPA adsorbed onto activated carbons at pH 11. This decreased adsorption of BPA can often be expected when the pH is greater than the pK_a because both targeted chemical and the adsorbent become negatively charged and, therefore, can experience increased electrostatic repulsion [44]. Regarding the *Q* response, the effect of pH was more obvious than the adsorbent dose as seen in Fig. 4(b). The enhancement in BPA at high doses can be ascribed to the increase in surface area and the availability of more adsorptive sites for the removal of BPA.

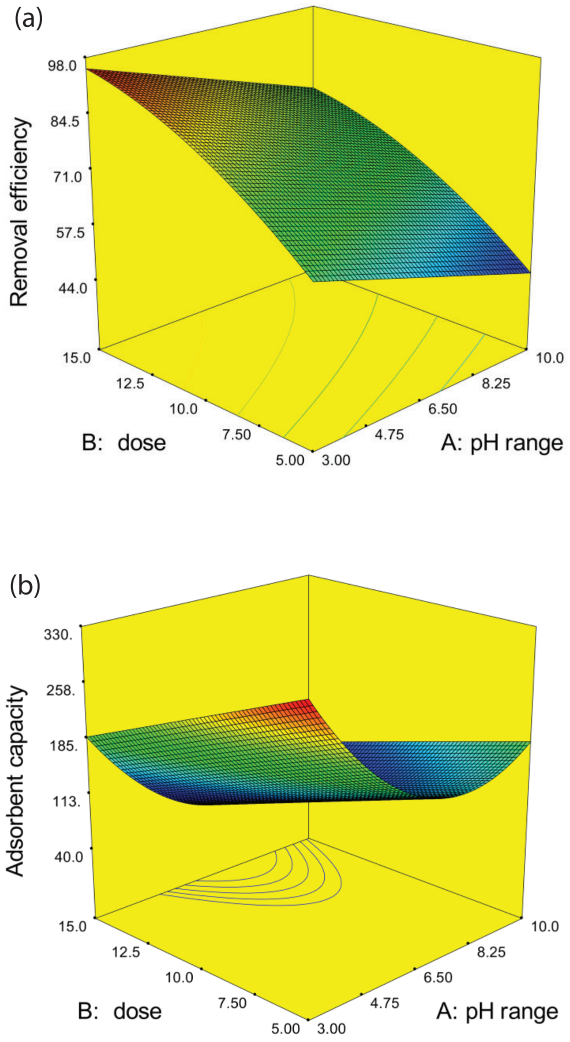

Fig. 4. RSM plots of (a) BPA removal efficiency (RV2%) and (b) adsorbent capacity (*Q*) considering the effect of pH and dosage.

3.2. Characterization

The synthesis conditions of CNMH were adopted in agreement with the earlier optimization to achieve the best production yield and removal efficiency. The CNMH produced under the optimal conditions was subsequently characterized with different techniques to assess structural and physicochemical properties.

3.2.1. Morphology and surface elemental analysis

FESEM and TEM images were taken for the PAC loaded with the catalysts particles, as seen in Figs. 5(a) and (b). The PAC structure, as seen in the FESEM image, shows the presence of irregular pores and the dominance of rough areas on the surface. Metal particles are dispersed on the surface of the PAC or trapped in the pores. Good distribution of Ni catalyst particles was observed on the PAC surface. The large surface area and high porosity of carbon support prevented the catalyst particle from coalescing and helped to produce an equal dispersion of catalyst particles [45,46].

After CH_4 decomposition at the optimized growth conditions (950°C, 20 min, and $H_2/CH_4 = 1.0$), the results (Figs. 6(a) and (b)) show that the grown CNMH have groove-like microstructures and are closely related to the porous structures and surface conditions of the PAC support [47]. Both large particles and small particles of nickel can be observed in Fig. 6(a). The small Ni particles may be generated from a mother particle, and dispersed throughout the entire surface. The FESEM reveals that the resulted CNMH have short, well-dispersed CNTs that are embedded in the pores of PAC. PAC possesses an abundant porous structure, hence the produced CNMH are liable to insert into the pores of the activated carbon.

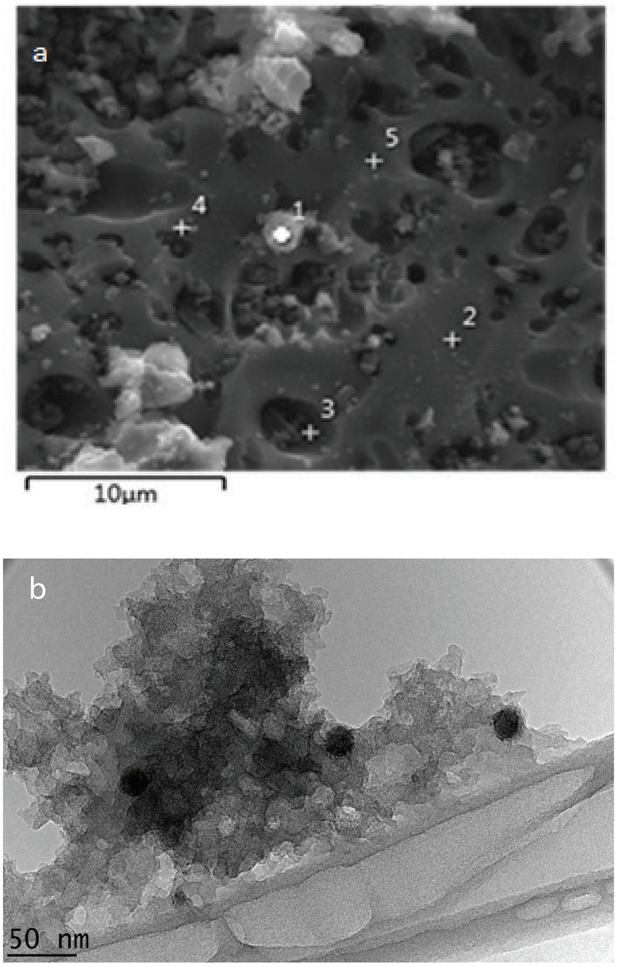

Fig. 5. (a) FESEM and (b) TEM images for Ni-PAC before growth reaction.

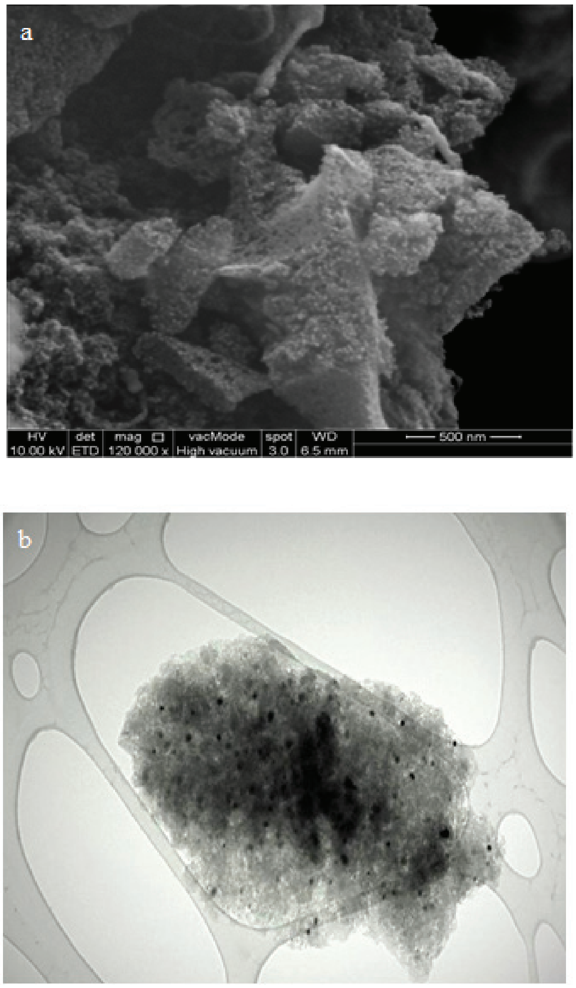

Fig. 6. (a) FESEM and (b) TEM images of CNMH obtained at optimal conditions.

Furthermore, conducting the growth at high reaction temperatures was suitable, and unlike other studies, the Ni catalyst, was not deactivated at higher temperatures [48,49]. The catalyst deactivation can be minimized by creating a PAC network around the Ni catalyst. These observations confirm that PAC is an effective support for Ni catalysts, even at high temperatures [50]. EDX analysis was performed for PAC, Ni-PAC, and CNMH produced under the optimized conditions (Figs. 7(a)–(c)). The elemental surface analysis of PAC substrate without catalyst impregnation (Fig. 7(a)), showed only carbon and oxygen-content. The highest percentage recorded for carbon was 91.6%. However, trace oxygen was detected in most of the samples because of oxygen adsorption from the surrounding environment during processing. In Ni-PAC (Fig. 7(b)), the nickel particles contributed to a total content of 2.1%. Other impurities were also present, including Si and Fe (<2.0%). The Ni content has fallen after growth to 0.9% as seen in the synthesized CNMH (Fig. 7(c)).

3.2.2. Raman spectroscopy

Fig. 8 shows Raman spectra of CNMH produced under optimized conditions. Two peaks were observed for all Raman spectra: the first at ~1,340 cm^{-1} (D band) and the second at ~1,600 cm^{-1} (G band) [20,51,52]. The D peak can be attributed to the disordered structure of graphite, while the graphitic layers produce a stretching C–C vibration characterized by the band G at higher ranges of Raman shift (1,500–1,600 cm^{-1}). Doping of Ni did not obstruct the overall structure of PAC, since it shows an I_D/I_G value of 0.81. No peaks were detected <400 cm^{-1}, suggesting that the as-prepared products possessed a multiwall structure [53]. The intensity ratio of D and G peaks was used as an index to characterize the level of material disorder. The intensity ratio for the CNMH structure was 0.93, similarly to a previously reported study [54]. Comparing the results of different studies of CH_4 decomposition, it can be concluded that the type of catalyst used for nanocarbon growth directly reflects the obtained structure and, therefore, the I_D/I_G ratio [55].

3.2.3. Thermogravimetric analysis

Oxidation temperatures of CNMs characterize thermal stability and describe the differences in their crystalline properties. Moreover, it can be argued that the remaining weight after exposure to high temperatures (>650°C) during thermogravimetric tests represents the catalyst residuals.

All samples exhibited single step degradation, as seen in Fig. 9, for the PAC, Ni-PAC, and CNMH obtained under optimized conditions. No weight loss was observed for PAC-Ni or CNMH at a degassing temperature range of 100°C–400°C, suggesting the absence of oxygenated functional groups [56].

Combustion began slightly below 550°C and ended at ~700°C. The majority of weight loss was detected in the range of 483°C–525°C. The same degradation trend was previously reported for CNT prepared on Ni catalyst CH_4 [57]. According to the TGA curves for PAC samples, the weight residue remaining after the test was about 7% reflecting impurities in the substrate. This percentage increased to 21% after the catalyst particles were embedded in the structure. However, after growth using CH_4, the remaining weight recorded above 650°C was approximately 14%. The reduction in residual percentage can be explained by the growth of CNMH on the catalyst surface and, thus, a change in the overall composition occurs.

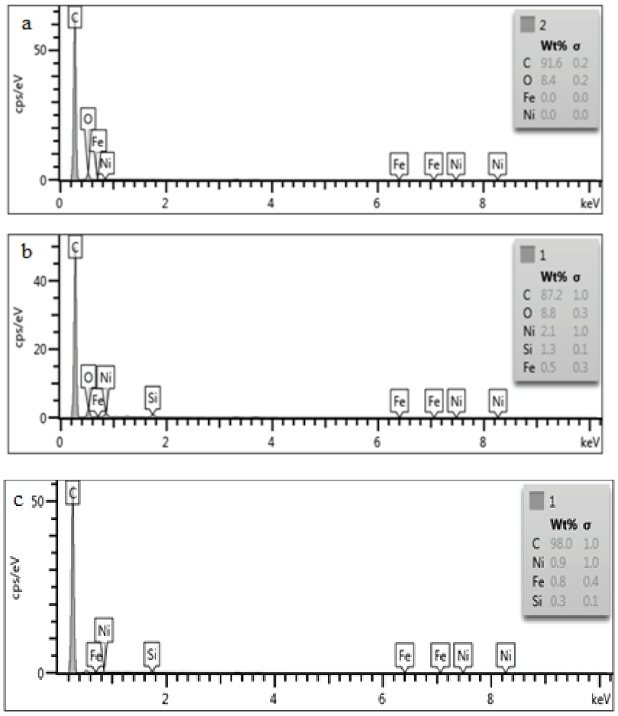

Fig. 7. EDX analyses for (a) PAC before catalyst impregnation, (b) Ni-PAC after impregnation, and (c) CNMH produced from CH_4 decomposition at optimal conditions.

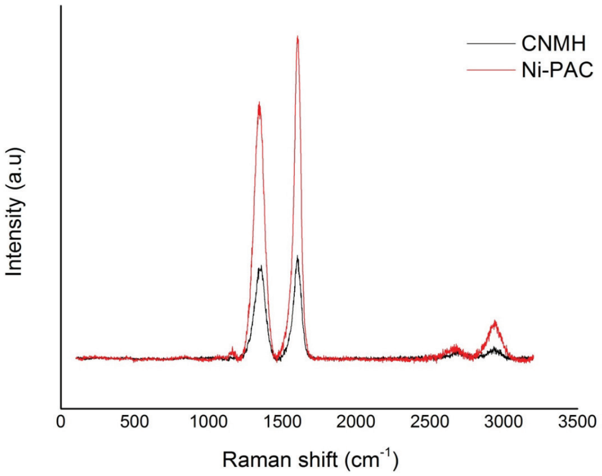

Fig. 8. Raman spectra of Ni-PAC and CNMH.

3.2.4. Fourier transform infrared spectroscopy

FTIR spectra were used to qualitatively evaluate the presence of functional groups on the CNMH surface. Fig. 10 represents the FTIR spectra of BPA and the CNMH used in the adsorption experiments before and after BPA removal. Obvious peaks were detected on the carbon surface before BPA adsorption within the wavenumber range of 2,800–2,900 cm^{-1}, reflecting the presence of C–H asymmetric and symmetric stretching vibrations [58].

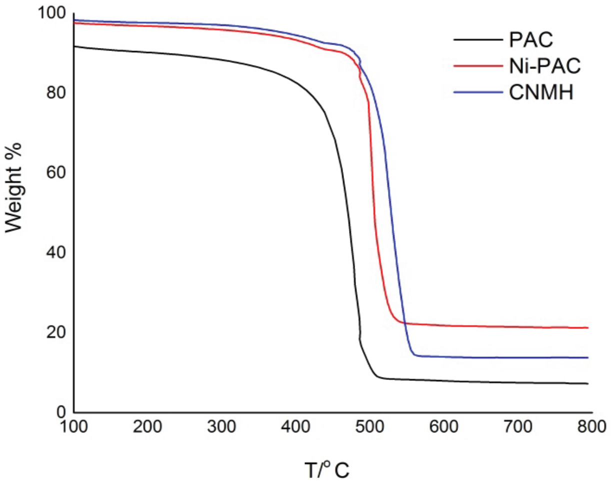

Fig. 9. TGA curves for PAC, Ni-PAC and CNMH.

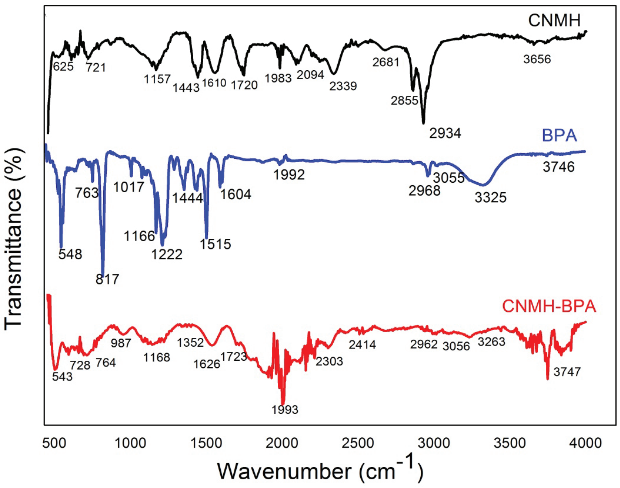

Fig. 10. FTIR spectra of BPA, CNMH before and after BPA adsorption.

The peak at 1,515 cm^{-1} reflects the existence of carbon double bonds (C=C) in the graphitic structure. The peaks at 1,200 and 3,450 cm^{-1} are associated with O–H. FTIR spectra of CNMH after BPA adsorption showed an intense peak at 3,747 cm^{-1} which can be attributed to the O–H stretching vibration originating from chemisorbed phenolic groups. Some characteristics related to BPA molecule were also detected on the adsorbent surface, including aromatic –C=C– bonds (at 1,600–1,400 cm^{-1}), benzene ring –C–H bonds (at 900–650 cm^{-1}), phenolic –C–O bonds (at 1,250 cm^{-1}), CH stretching vibration (at 2,990 cm^{-1}), and –CH_3 stretching vibrations at 1,387 cm^{-1}. The band at ~1,710 cm^{-1} with a high intensity can be attributed to the stretching vibration of a carboxylic group [59].

3.2.5. Surface analysis

The surface plays an important role in the adsorption of phenolic compounds by CNMs. Porosity and BET surface area were studied via nitrogen adsorption–desorption experiments [60]. Various samples were analyzed for their surface area, including PAC, Ni-PAC, and CNMH (Table 5).

The loading of Ni onto the PAC support has caused to decrease the pore volume of the support, likely due to the blockage of the PAC pores by the impregnated catalyst resulting, therefore, in a reduced surface area. The BET surface area of the CNMH (164.6 m^2 g^{-1}) produced under optimized conditions led to significant enhancements in surface area, due to the additional active surface added on the PAC. The total pore volume of CNMH reached 0.29 cm^3 g^{-1} compared with PAC (0.09 cm^3 g^{-1}). Thus, an excellent sorption capacity is expected for our material due to the enhancement of the surface area.

3.2.6. Zeta potential

Dispersibility of CNMs in aqueous media reflects the wettability of their surfaces in an indirect way. The zeta potential is the electric potential in the interfacial double layer, which is important in measuring the surface charge of the material. Stability of dispersions is caused by repulsion forces between suspended particles in the solution, within which the absolute value of zeta potential is higher than 30 mV [61]. It was found that the CNMH produced with CH_4 exhibited a lower zeta potential, compared with the structures produced from other carbon sources [62]. Table 6 shows the zeta potential results of PAC, Ni-PAC, and CNMH produced under optimized conditions. The positive value in the case of CNMH might indicate the dominance of positively charged functional groups on the surface. This can enhance the attraction to phenolate ions possessing a negative charge, thereby boosting the adsorbing capability of the CNMH.

Table 5
Summary of BET results for PAC, Ni-PAC, and CNMH

Property	PAC	Ni-PAC	CNMH
BET surface area (m^2 g^{-1})	101.1	97.2	164.6
Total pore volume (cm^3 g^{-1})	0.09	0.07	0.29
Average pore diameter (Å)	34.89	21.29	96.19

3.3. BPA adsorption

3.3.1. Kinetic studies

The kinetic studies were conducted for BPA adsorption (50 mg L^{-1}) at the optimal conditions. The kinetic models of pseudo-first-order, pseudo-second-order, and intraparticle diffusion were employed to correlate with the experimental data on BPA adsorption to the prepared CNMH and deduce the best fitting model. The characteristics obtained from each model are summarized in Table 3.

The pseudo-first-order kinetic model was used to calculate the rate constant k_1 and q_e values from the slope and intercept of the linear plot of $\ln(q_e - q_t)$ vs. t. The R^2 value for this model was 0.8247 (Fig. 11(a)) and the model did not effectively describe the experimental adsorption data. The sorption kinetics following the pseudo-second-order model were also determined and the plot of t/q_t vs. t presents a good match between this model and the experimental data (R^2 = 0.999), Fig. 11(b)), which indicates that the kinetics of BPA adsorption process depend on the adsorbent and adsorbate and could be controlled by chemisorption involving valence forces through sharing or exchange of electrons [63]. The R^2 value of the intraparticle diffusion model presented in Fig. 11(c) was 0.821. It shows two region plots, the first region is a straight line correlated with the diffusion mechanism and the second one is attributed to the equilibrium stage, where intraparticle diffusion starts [64]. Based on these results, the adsorption kinetics of CNMH clearly follows the pseudo-second-order model with greater conformity, compared with the pseudo-first-order and intraparticle diffusion models. This behavior agrees with several previously reported studies which used carbonaceous adsorbents for BPA removal [28,33,65].

3.3.2. Adsorption isotherms

To describe adsorption of BPA onto the surface of CNMH, Langmuir, Freundlich, and Temkin isotherm models were used. Table 4 lists the equations of these models and the findings obtained by applying each model.

The well-known linearized form of the Langmuir equation is presented in Table 4. In the equation, C_e (mg L^{-1}) is the equilibrium concentration of BPA, q_e (mg g^{-1}) is the amount of BPA adsorbed per unit mass of the adsorbent. K_L and Q_m are Langmuir constants related to adsorption equilibrium constant and maximum adsorption capacity, respectively. The value of the dimensionless constant equilibrium parameter (R_L) can be used to indicate the essential features and type of Langmuir isotherm in the following manner: unfavorable ($R_L > 1$), linear ($R_L = 1$), favorable ($0 < R_L < 1$) or irreversible ($R_L = 0$). Eq. (8) was used to calculate R_L value [66].

Table 6
Zeta potential results for PAC and the different carbon structures produced

Sample	Zeta potential (mV)
PAC	–42.6
Ni-PAC	+1.67
CNMH	+9.64

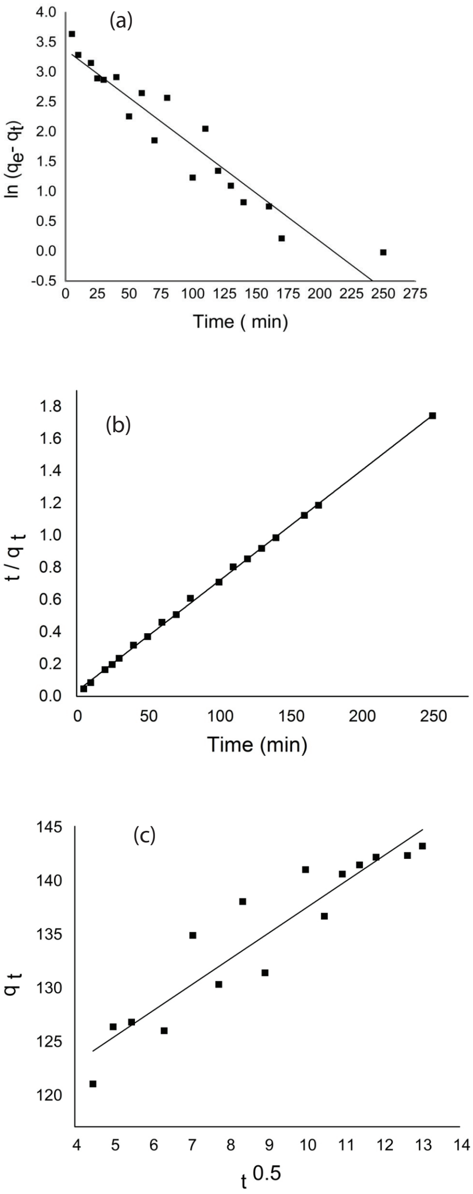

Fig. 11. Fittings of different kinetics models for BPA adsorption onto CNMH. (a) Pseudo-first-order, (b) pseudo-second-order, and (c) intraparticle diffusion at optimum conditions.

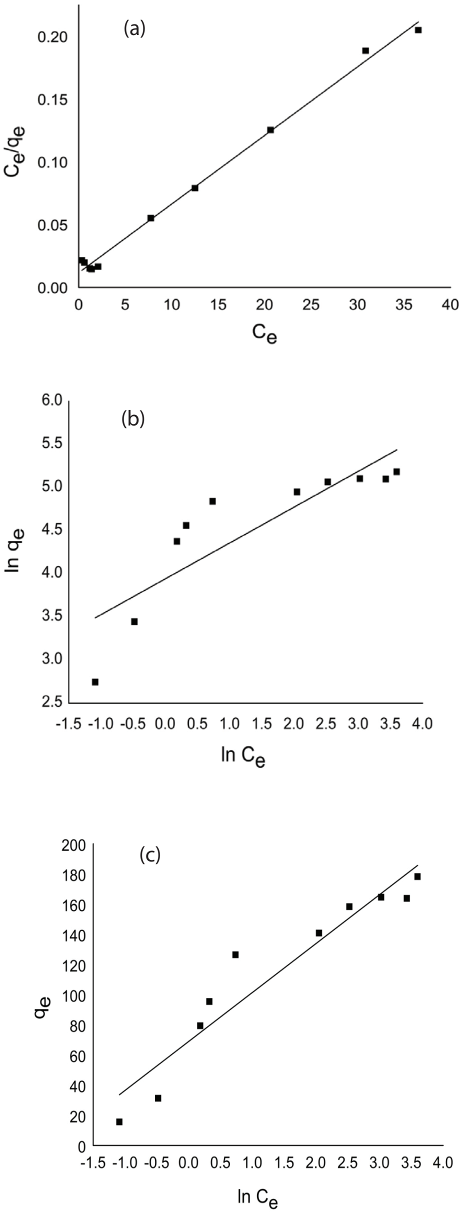

Fig. 12. Isotherm plots for BPA adsorption onto CNMH following the linearized forms of (a) Langmuir, (b) Freundlich, and (c) Temkin models.

$$R_L = \frac{1}{1 + K_L C_i} \tag{8}$$

Following the Langmuir isotherm model, the constant K_L and the maximum theoretical adsorbent capacity Q_m were extracted from the C_e/q_e vs. C_e plot (Fig. 12(a)).

Freundlich isotherm can be described by the linearized equation as shown in Table 4, in which K_F and n are Freundlich isotherm constants. The distribution coefficient K_F represents the amount of BPA adsorbed onto adsorbent per unit equilibrium concentration. While the factor $1/n$ defines the heterogeneity of the adsorbent surface. As its value approaches zero, it indicates that the adsorbent surface is becoming more heterogeneous [67]. A plot of logq_e vs. logC_e was used to describe the Freundlich isotherm, as shown in Fig. 12(b).

Moreover, the Temkin isotherm equation presented in Table 4 was examined for its applicability in describing the experimental results. The parameters of the Temkin equations are B (dimensionless) = RT/B. B is the Temkin constant related to the heat of adsorption (J mol^{-1}), R is the gas constant (8.314 J mol^{-1} K^{-1}), T is the absolute temperature in Kelvin, and K_T is the Temkin isotherm equilibrium binding constant (L mg^{-1}) [68]. The Temkin isotherm model is depicted in Fig. 12(c).

The values of R_L and n for the CNMH adsorbent confirmed the adsorption favorability of BPA for both the Langmuir and Freundlich isotherms under experimental conditions [69]. However, the Langmuir model produced the best fit with a high correlation coefficient R^2 (0.994), indicating a monolayer adsorption of BPA onto the CNMH surface. On the other hand, according to the Freundlich n value ($n > 1$), the adsorptive behavior is dominated by a physical adsorption process [70]. Similar isotherm results were reported for the adsorption of BPA onto activated carbon derived from rice straw agricultural waste [71]. Table 7 provides a comparison of the maximum adsorption capacity of BPA onto several adsorbents. In comparison with previous works, CNMH can be considered as a promising adsorbent for BPA removal from aqueous solution.

3.4. Mechanisms

The adsorption of BPA onto the CNMH adsorbent was greatly affected by the characteristics of the adsorbent, removal conditions, as well as the molecular properties of BPA. Thus, CNMH has oxygen-functional groups, which enhance the dispersibility of CNMH in water. Moreover, –OH is an electron-donating functional group that can increase the sorption affinity of BPA by increasing the π-donating strength of the host aromatic ring [72]. The molecular size, pK_a (pK_a = 9.5 for BPA), and easily rotating structure of BPA influences its affinity toward CNMH [73]. The wedging of BPA into the groove regions of the adsorbent is allowed by the structure of BPA molecule. The π–π interactions between the benzene rings of BPA and the graphene planes includes the polar and charge interactions that may be responsible for the adsorption of BPA onto CNMH. Moreover, the pH of the background solution is another major factor controlling adsorption. BPA is an organic acid and the non-dissociated species form dominates in acidic solutions. Lin and Xing [72] reported that decreases in adsorption affinities for phenolic compounds over their pK_a values could be attributed to the increased electrostatic repulsion between dissociated adsorbates and negatively charged MWCNTs. In addition, at pH 3 the methyl groups on BPA are protonated and increase the electron density of resonating π electrons in the benzene ring, enhancing the attraction between positive CNMH surfaces. Herein, the adsorption mechanism of BPA was governed by the π–π interaction effects, since the highest removal efficiency was demonstrated at pH 3.2, which is less than the pK_a value of BPA [73].

Table 7
Previously reported adsorption capacities of various adsorbents for Bisphenol A

Adsorbent	Adsorption capacity Q_e (mg g^{-1})	Reference
Hydrophobic Y type zeolite	111.11	[8]
SWCNTs	22.6–44.8	[44]
Powdered activated carbon (PAC)	129.6	[74]
Organo-montmorillonite	151.522	[75]
Molecularly imprinted polymers (MMIPs)	142.9	[76]
Cross-linked cyclodextrin	84	[77]
Metal-organic framework	55.6	[78]
Reduced graphene		
TrG	96.2	[28]
HrG	81.3	
Oxide graphene	58.2	[79]
As-prepared CNMH	181.8	Present work

4. Conclusion

This study investigates the growth of hybrid multistructure material (CNMH) from the decomposition of methane using CVD method. The prepared material was utilized as a novel adsorbent for BPA removal from aqueous solution. Optimization studies using a center composite design and RSM were conducted to evaluate the growth parameters which achieve the highest growth yield and BPA removal efficiency. The optimal CVD production conditions were found to be 950°C as a growth temperature, 20 min reaction time, and a 1.0 feed gases ratio (H_2/CH_4). CNMH produced under optimal conditions showed excellent removal efficiency at pH 3.2, with an adsorbent dosage of 15 mg and contact time of 120 min. The BPA adsorption system was fitted with pseudo-second-order kinetics and the maximum adsorbent capacity determined using the Langmuir adsorption isotherm was 181.8 mg g^{-1}. The relatively strong π–π interaction and hydrogen-bonding between the benzene and rings hydroxyl groups of BPA could be the origin of the strong adsorption affinity for BPA. The growth of CNMH on activated carbon consists of a multistructure network and, unlike other CNMs prepared on metal oxides or silica substrates can be used directly in the adsorption processes without removing the substrate from the product. Our findings contribute toward successful developing of hybrid CNM which can be used as an efficient adsorbent in water remediation.

Acknowledgment

The authors express their thanks to the University of Malaya UMRG (RP017A-13AET) and to the Postgraduate Research Grant (PG243-2015B) for funding this research.

References

[1] S. Li, Y. Gong, Y. Yang, C. He, L. Hu, L. Zhu, L. Sun, D. Shu, Recyclable CNTs/Fe_3O_4 magnetic nanocomposites as adsorbents to remove bisphenol A from water and their regeneration, Chem. Eng. J., 260 (2015) 231–239.

[2] B. Pan, B. Xing, Adsorption mechanisms of organic chemicals on carbon nanotubes, Environ. Sci. Technol., 42 (2008) 9005–9013.

[3] C. Ampelli, S. Perathoner, G. Centi, Carbon-based catalysts: opening new scenario to develop next-generation nano-engineered catalytic materials, Chin. J. Catal., 35 (2014) 783–791.

[4] A. Szabó, C. Perri, A. Csató, G. Giordano, D. Vuono, J.B. Nagy, Synthesis methods of carbon nanotubes and related materials, Materials, 3 (2010) 3092–3140.

[5] N.K. Dey, E.M. Hong, K.H. Choi, Y.D. Kim, J.-H. Lim, K.H. Lee, D.C. Lim, Growth of carbon nanotubes on carbon fiber by thermal CVD using Ni nanoparticles as catalysts, Procedia Eng., 36 (2012) 556–561.

[6] M.K. AlOmar, M.A. Alsaadi, M. Hayyan, S. Akib, M.A. Hashim, Functionalization of CNTs surface with phosphonuim based deep eutectic solvents for arsenic removal from water, Appl. Surf. Sci., 389 (2016) 216–226.

[7] K. Hernadi, A. Fonseca, P. Piedigrosso, M. Delvaux, J. Nagy, D. Bernaerts, J. Riga, Carbon nanotubes production over Co/silica catalysts, Catal. Lett., 48 (1997) 229–238.

[8] W.-T. Tsai, H.-C. Hsu, T.-Y. Su, K.-Y. Lin, C.-M. Lin, Adsorption characteristics of bisphenol-A in aqueous solutions onto hydrophobic zeolite, J. Colloid Interface Sci., 299 (2006) 513–519.

[9] S. Salehinia, S.M. Ghoreishi, F. Maya, V. Cerdà, Hydrophobic magnetic montmorillonite composite material for the efficient adsorption and microextraction of bisphenol A from water samples, J. Environ. Chem. Eng., 4 (2016) 4062–4071.

[10] H. Wang, H. Ma, W. Zheng, D. An, C. Na, Multifunctional and recollectable carbon nanotube ponytails for water purification, ACS Appl. Mater. Interfaces, 6 (2014) 9426–9434.

[11] M. Ghaedi, A.G. Nasab, S. Khodadoust, M. Rajabi, S. Azizian, Application of activated carbon as adsorbents for efficient removal of methylene blue: kinetics and equilibrium study, J. Ind. Eng. Chem., 20 (2014) 2317–2324.

[12] S. Bigdeli, S. Fatemi, Fast carbon nanofiber growth on the surface of activated carbon by microwave irradiation: a modified nano-adsorbent for deep desulfurization of liquid fuels, Chem. Eng. J., 269 (2015) 306–315.

[13] D. Chen, K.O. Christensen, E. Ochoa-Fernández, Z. Yu, B. Tøtdal, N. Latorre, A. Monzón, A. Holmen, Synthesis of carbon nanofibers: effects of Ni crystal size during methane decomposition, J. Catal., 229 (2005) 82–96.

[14] W. Cho, M. Schulz, V. Shanov, Growth termination mechanism of vertically aligned centimeter long carbon nanotube arrays, Carbon, 69 (2014) 609–620.

[15] D. Lopez, I.Y. Abe, I. Pereyra, Temperature effect on the synthesis of carbon nanotubes and core–shell Ni nanoparticle by thermal CVD, Diamond Relat. Mater., 52 (2015) 59–65.

[16] N.T. Abdel-Ghani, G.A. El-Chaghaby, F.S. Helal, Individual and competitive adsorption of phenol and nickel onto multiwalled carbon nanotubes, J. Adv. Res., 6 (2015) 405–415.

[17] S. Amelinckx, X. Zhang, D. Bernaerts, X. Zhang, V. Ivanov, J. Nagy, A formation mechanism for catalytically grown helix-shaped graphite nanotubes, Opt. Commun., 2664 (1994) 977.

[18] N. Sankararamakrishnan, M. Jaiswal, N. Verma, Composite nanofloral clusters of carbon nanotubes and activated alumina: an efficient sorbent for heavy metal removal, Chem. Eng. J., 235 (2014) 1–9.

[19] M.A. AlSaadi, A. Al Mamun, M.Z. Alam, M.K. Amosa, M.A. Atieh, Removal of cadmium from water by CNT–PAC composite: effect of functionalization, Nano, 11 (2016) 1650011.

[20] K. Hernadi, A. Fonseca, J.B. Nagy, A. Siska, I. Kiricsi, Production of nanotubes by the catalytic decomposition of different carbon-containing compounds, Appl. Catal., A, 199 (2000) 245–255.

[21] A. Abo-Hamad, M.A. AlSaadi, M. Hayyan, I. Juneidi, M.A. Hashim, Ionic liquid-carbon nanomaterial hybrids for electrochemical sensor applications: a review, Electrochim. Acta, 193 (2016) 321–343.

[22] S. Zheng, Z. Sun, Y. Park, G.A. Ayoko, R.L. Frost, Removal of bisphenol A from wastewater by Ca-montmorillonite modified with selected surfactants, Chem. Eng. J., 234 (2013) 416–422.

[23] M.H. Dehghani, M. Ghadermazi, A. Bhatnagar, P. Sadighara, G. Jahed-Khaniki, B. Heibati, G. McKay, Adsorptive removal of endocrine disrupting bisphenol A from aqueous solution using chitosan, J. Environ. Chem. Eng., 4 (2016) 2647–2655.

[24] J. Xu, L. Wang, Y. Zhu, Decontamination of bisphenol A from aqueous solution by graphene adsorption, Langmuir, 28 (2012) 8418–8425.

[25] M. Song, X. Tang, J. Xu, L. Yu, Y. Wei, The formation of novel carbon/carbon composite by chemical vapor deposition: an efficient adsorbent for enhanced desulfurization performance, J. Anal. Appl. Pyrolysis, 118 (2016) 34–41.

[26] A.S. Adeleye, J.R. Conway, K. Garner, Y. Huang, Y. Su, A.A. Keller, Engineered nanomaterials for water treatment and remediation: costs, benefits, and applicability, Chem. Eng. J., 286 (2016) 640–662.

[27] M. de la Luz-Asunción, V. Sánchez-Mendieta, A. Martínez-Hernández, V. Castaño, C. Velasco-Santos, Adsorption of phenol from aqueous solutions by carbon nanomaterials of one and two dimensions: kinetic and equilibrium studies, J. Nanomater., 16 (2015) 422.

[28] J. Kwon, B. Lee, Bisphenol A adsorption using reduced graphene oxide prepared by physical and chemical reduction methods, Chem. Eng. Res. Des., 104 (2015) 519–529.

[29] M.K. AlOmar, M.A. Alsaadi, M. Hayyan, S. Akib, M. Ibrahim, M.A. Hashim, Allyl triphenyl phosphonium bromide based DES-functionalized carbon nanotubes for the removal of mercury from water, Chemosphere, 167 (2017) 44–52.

[30] Y.B. Onundi, A. Mamun, M. Al Khatib, M. Al Saadi, A. Suleyman, Heavy metals removal from synthetic wastewater by a novel nano-size composite adsorbent, Int. J. Environ. Sci. Technol., 8 (2011) 799.

[31] M. Hussein, S. Zakarya, S. Sarijo, Z. Zainal, Parameter optimisation of carbon nanotubes synthesis via hexane decomposition over minerals generated from *Anadara granosa* shells as the catalyst support, J. Nanomater., 2012 (2012) 90.

[32] M.A. AlSaadi, A. Al-Mamun, S.A. Muyibi, M.Z. Alam, I. Sopyan, M.A. Atieh, Y.M. Ahmed, Synthesis of various carbon nanomaterials (CNMs) on powdered activated carbon, Afr. J. Biotechnol., 10 (2011) 18892–18905.

[33] Q. Sui, J. Huang, Y. Liu, X. Chang, G. Ji, S. Deng, T. Xie, G. Yu, Rapid removal of bisphenol A on highly ordered mesoporous carbon, J. Environ. Sci., 23 (2011) 177–182.

[34] Y. Dong, D. Wu, X. Chen, Y. Lin, Adsorption of bisphenol A from water by surfactant-modified zeolite, J. Colloid Interface Sci., 348 (2010) 585–590.

[35] M. Amini, H. Younesi, N. Bahramifar, A.A.Z. Lorestani, F. Ghorbani, A. Daneshi, M. Sharifzadeh, Application of response surface methodology for optimization of lead biosorption in an aqueous solution by *Aspergillus niger*, J. Hazard. Mater., 154 (2008) 694–702.

[36] L.A. Ramírez-Montoya, V. Hernández-Montoya, M.A. Montes-Morán, Optimizing the preparation of carbonaceous adsorbents for the selective removal of textile dyes by using Taguchi methodology, J. Anal. Appl. Pyrolysis, 109 (2014) 9–20.

[37] V. Angulakshmi, N. Sivakumar, S. Karthikeyan, Response surface methodology for optimizing process parameters for synthesis of carbon nanotubes, J. Environ. Nanotechnol., 1 (2012) 40–45.

[38] A. Khuri, J. Cornell, Response Surfaces: Designs and Analyses, Marcel Dekker Inc., New York (1987).

[39] K. Kalantari, M.B. Ahmad, H.R. Fard Masoumi, K. Shameli, M. Basri, R. Khandanlou, Rapid and high capacity adsorption of heavy metals by Fe_3O_4/montmorillonite nanocomposite using response surface methodology: preparation, characterization, optimization, equilibrium isotherms, and adsorption kinetics study, J. Taiwan Inst. Chem. Eng., 49 (2015) 192–198.

[40] M. Roosta, M. Ghaedi, A. Daneshfar, R. Sahraei, A. Asghari, Optimization of the ultrasonic assisted removal of methylene blue by gold nanoparticles loaded on activated carbon using experimental design methodology, Ultrason. Sonochem., 21 (2014) 242–252.

[41] J.C. Lazo-Cannata, A. Nieto-Márquez, A. Jacoby, A.L. Paredes-Doig, A. Romero, M.R. Sun-Kou, J.L. Valverde, Adsorption of phenol and nitrophenols by carbon nanospheres: effect of pH and ionic strength, Sep. Purif. Technol., 80 (2011) 217–224.

[42] G. Bayramoglu, M.Y. Arica, G. Liman, O. Celikbicak, B. Salih, Removal of bisphenol A from aqueous medium using molecularly surface imprinted microbeads, Chemosphere, 150 (2016) 275–284.

[43] G. Liu, J. Ma, X. Li, Q. Qin, Adsorption of bisphenol A from aqueous solution onto activated carbons with different modification treatments, J. Hazard. Mater., 164 (2009) 1275–1280.

[44] L. Joseph, Q. Zaib, I.A. Khan, N.D. Berge, Y.-G. Park, N.B. Saleh, Y. Yoon, Removal of bisphenol A and 17α-ethinyl estradiol from landfill leachate using single-walled carbon nanotubes, Water Res., 45 (2011) 4056–4068.

[45] F. Zhou, Q. Liu, W. Zhang, J. Gu, S. Zhu, D. Zhang, Fabrication of 3D carbon nanotube/porous carbon hybrid materials, J. Mater. Sci., 49 (2014) 548–557.

[46] G. Allaedini, S.M. Tasirin, P. Aminayi, Synthesis of Fe–Ni–Ce trimetallic catalyst nanoparticles via impregnation and co-precipitation and their application to dye degradation, Chem. Pap., 70 (2015) 231–242.

[47] Y.C. Jung, B. Bhushan, Mechanically durable carbon nanotube–composite hierarchical structures with superhydrophobicity, self-cleaning, and low-drag, ACS Nano, 3 (2009) 4155–4163.

[48] S.-P. Chai, K.-Y. Lee, S. Ichikawa, A.R. Mohamed, Synthesis of carbon nanotubes by methane decomposition over Co–Mo/Al_2O_3: process study and optimization using response surface methodology, Appl. Catal., A, 396 (2011) 52–58.

[49] J.I. Villacampa, C. Royo, E. Romeo, J.A. Montoya, P. Del Angel, A. Monzon, Catalytic decomposition of methane over Ni-Al_2O_3 coprecipitated catalysts: reaction and regeneration studies, Appl. Catal., A, 252 (2003) 363–383.

[50] F. Taleshi, A. Hosseini, M. Mohammadi, M. Pashaee, Effect of hydrocarbon gas on synthesis and diameter of carbon nanotubes, Indian J. Phys., 87 (2013) 873–877.

[51] W. Li, H. Zhang, C. Wang, Y. Zhang, L. Xu, K. Zhu, S. Xie, Raman characterization of aligned carbon nanotubes produced by thermal decomposition of hydrocarbon vapor, Appl. Phys. Lett., 70 (1997) 2684–2686.

[52] M.K. AlOmar, M.A. Alsaadi, M.M. Aljumaily, S. Akib, T.M. Jassam, M.A. Hashim, *N*,*N*-Diethylethanolammonium chloride-based DES-functionalized carbon nanotubes for arsenic removal from aqueous solution, Desal. Wat. Treat., 74 (2017) 163–173.

[53] J. Ziebro, I. Łukasiewicz, E. Borowiak-Palen, B. Michalkiewicz, Low temperature growth of carbon nanotubes from methane catalytic decomposition over nickel supported on a zeolite, Nanotechnology, 21 (2010) 145308.

[54] S. Takenaka, S. Kobayashi, H. Ogihara, K. Otsuka, Ni/SiO_2 catalyst effective for methane decomposition into hydrogen and carbon nanofiber, J. Catal., 217 (2003) 79–87.

[55] W. Qian, T. Liu, F. Wei, Z. Wang, Y. Li, Enhanced production of carbon nanotubes: combination of catalyst reduction and methane decomposition, Appl. Catal., A, 258 (2004) 121–124.

[56] A. Hruzewicz-Kołodziejczyk, V.P. Ting, N. Bimbo, T.J. Mays, Improving comparability of hydrogen storage capacities of nanoporous materials, Int. J. Hydrogen Energy, 37 (2012) 2728–2736.

[57] D. Bom, R. Andrews, D. Jacques, J. Anthony, B. Chen, M.S. Meier, J.P. Selegue, Thermogravimetric analysis of the oxidation of multiwalled carbon nanotubes: evidence for the role of defect sites in carbon nanotube chemistry, Nano Lett., 2 (2002) 615–619.

[58] J.R. Koduru, L.P. Lingamdinne, J. Singh, K.-H. Choo, Effective removal of bisphenol A (BPA) from water using a goethite/activated carbon composite, Process Saf. Environ. Prot., 103 (2016) 87–96.

[59] C. Jung, A. Son, N. Her, K.-D. Zoh, J. Cho, Y. Yoon, Removal of endocrine disrupting compounds, pharmaceuticals, and personal care products in water using carbon nanotubes: a review, J. Ind. Eng. Chem., 27 (2015) 1–11.

[60] K.A. Shah, B.A. Tali, Synthesis of carbon nanotubes by catalytic chemical vapour deposition: a review on carbon sources, catalysts and substrates, Mater. Sci. Semicond. Process., 41 (2016) 67–82.

[61] B. Bestani, N. Benderdouche, B. Benstaali, M. Belhakem, A. Addou, Methylene blue and iodine adsorption onto an activated desert plant, Bioresour. Technol., 99 (2008) 8441–8444.

[62] T. Hiraoka, T. Kawakubo, J. Kimura, R. Taniguchi, A. Okamoto, T. Okazaki, T. Sugai, Y. Ozeki, M. Yoshikawa, H. Shinohara, Selective synthesis of double-wall carbon nanotubes by CCVD of acetylene using zeolite supports, Chem. Phys. Lett., 382 (2003) 679–685.

[63] Y.-S. Ho, G. McKay, Pseudo-second order model for sorption processes, Process Biochem., 34 (1999) 451–465.

[64] F. Cao, P. Bai, H. Li, Y. Ma, X. Deng, C. Zhao, Preparation of polyethersulfone–organophilic montmorillonite hybrid particles for the removal of bisphenol A, J. Hazard. Mater., 162 (2009) 791–798.

[65] L. Joseph, J. Heo, Y.-G. Park, J.R.V. Flora, Y. Yoon, Adsorption of bisphenol A and 17α-ethinyl estradiol on single walled carbon nanotubes from seawater and brackish water, Desalination, 281 (2011) 68–74.

[66] W.J. Weber, J.C. Morris, Kinetics of adsorption on carbon from solution, J. Sanit. Eng. Div., 89 (1963) 31–60.

[67] M.M. Nassar, Y.H. Magdy, A.E.H. Daifullah, H. Kelany, Mass transfer and adsorption kinetics of phenolic compounds onto activated carbon prepared from rice husk, Adsorpt. Sci. Technol., 26 (2008) 157–167.

[68] C.-Y. Kuo, Comparison with as-grown and microwave modified carbon nanotubes to removal aqueous bisphenol A, Desalination, 249 (2009) 976–982.

[69] Y. Zhou, L. Chen, P. Lu, X. Tang, J. Lu, Removal of bisphenol A from aqueous solution using modified fibric peat as a novel biosorbent, Sep. Purif. Technol., 81 (2011) 184–190.

[70] B. Hameed, A. Ahmad, N. Aziz, Isotherms, kinetics and thermodynamics of acid dye adsorption on activated palm ash, Chem. Eng. J., 133 (2007) 195–203.

[71] K.-L. Chang, J.-F. Hsieh, B.-M. Ou, M.-H. Chang, W.-Y. Hseih, J.-H. Lin, P.-J. Huang, K.-F. Wong, S.-T. Chen, Adsorption studies on the removal of an endocrine-disrupting compound (Bisphenol A) using activated carbon from rice straw agricultural waste, Sep. Sci. Technol., 47 (2012) 1514–1521.

[72] D. Lin, B. Xing, Adsorption of phenolic compounds by carbon nanotubes: role of aromaticity and substitution of hydroxyl groups, Environ. Sci. Technol., 42 (2008) 7254–7259.

[73] O.G. Apul, T. Karanfil, Adsorption of synthetic organic contaminants by carbon nanotubes: a critical review, Water Res., 68 (2015) 34–55.

[74] I. Bautista-Toledo, M. Ferro-Garcia, J. Rivera-Utrilla, C. Moreno-Castilla, F. Vegas Fernandez, Bisphenol A removal from water by activated carbon. Effects of carbon characteristics and solution chemistry, Environ. Sci. Technol., 39 (2005) 6246–6250.

[75] Y. Park, Z. Sun, G.A. Ayoko, R.L. Frost, Bisphenol A sorption by organo-montmorillonite: implications for the removal of organic contaminants from water, Chemosphere, 107 (2014) 249–256.

[76] W. Guo, W. Hu, J. Pan, H. Zhou, W. Guan, X. Wang, J. Dai, L. Xu, Selective adsorption and separation of BPA from aqueous solution using novel molecularly imprinted polymers based on kaolinite/Fe_3O_4 composites, Chem. Eng. J., 171 (2011) 603–611.

[77] H. Yamasaki, Y. Makihata, K. Fukunaga, Efficient phenol removal of wastewater from phenolic resin plants using crosslinked cyclodextrin particles, J. Chem. Technol. Biotechnol., 81 (2006) 1271–1276.

[78] F.-X. Qin, S.-Y. Jia, Y. Liu, H.-Y. Li, S.-H. Wu, Adsorptive removal of bisphenol A from aqueous solution using metal-organic frameworks, Desal. Wat. Treat., 54 (2015) 93–102.

[79] Z. Jin, X. Wang, Y. Sun, Y. Ai, X. Wang, Adsorption of 4-n-nonylphenol and bisphenol-A on magnetic reduced graphene oxides: a combined experimental and theoretical studies, Environ. Sci. Technol., 49 (2015) 9168–9175.

Supplementary material

Table S1
Experimental CCD data for the synthesis parameters

Sample ID	*A* (Temperature, °C)	*B* (Time, min)	*C* (Gas ratio)	CNMHY (Yield, %)	RV1% (BPA removal efficiency)
A1	850.0	40.0	2.5	10.3	70.4
A2	950.0	20.0	4.0	15.9	83.5
A3	750.0	60.0	4.0	11.7	85.1
A4	850.0	20.0	2.5	11.6	78.4
A5	1,000.0	20.0	1.0	27.7	5.6
A6	750.0	20.0	4.0	12.9	78.0
A7	750.0	60.0	1.0	9.7	76.2
A8	950.0	60.0	4.0	21.4	42.1
A9	750.0	40.0	2.5	9.1	76.3
A10	950.0	20.0	1.0	22.9	87.6
A11	850.0	40.0	4.0	8.4	83.9
A12	950.0	60.0	1.0	37.3	14.7
A13	850.0	60.0	2.5	14.1	78.5
A14	750.0	20.0	1.0	10.02	60.8

Table S2
ANOVA results for growth optimization to obtain the best yield (CNMHY)

Source	Sum of squares	df	Mean square	*F* Value	*p* Value Prob > *F*
Model	2.71	10	0.27	210.54	0.0005
A	1.18	1	1.18	914.87	<0.0001
B	0.074	1	0.074	57.22	0.0048
C	0.068	1	0.068	52.94	0.0054
AB	0.11	1	0.11	84.02	0.0027
AC	0.23	1	0.23	178.35	0.0009
BC	8.713×10^{-3}	1	8.713×10^{-3}	6.76	0.0804
A^2	0.090	1	0.009	69.48	<0.0036
B^2	0.043	1	0.043	33.05	0.0105
C^2	1.144×10^{-3}	1	1.144×10^{-3}	0.89	0.4158
A^2C	0.048	1	0.048	37.40	0.0088

R^2 = 0.9986, Adj. R^2 = 0.9938, Adeq. precision = 46.609.
A, temperature (°C); *B*, time (min); and *C*, gas ratio.

Table S3
ANOVA results for growth optimization to obtain the best BPA removal efficiency (RV1%)

Source	Sum of squares	df	Mean square	*F* Value	*p* Value Prob > *F*
Model	8,494.09	7	1,213.44	13.87	0.0025
A	510.83	1	510.83	5.84	0.0521
B	840.89	1	840.89	9.61	0.0211
C	352.03	1	352.03	4.02	0.0917
AB	2,339.28	1	2,339.28	26.74	0.0021
AC	0.98	1	0.98	0.011	0.9192
A^2	275.25	1	275.25	3.15	0.1265
A^3	1,324.83	1	1,324.83	14.14	0.0081

R^2 = 0.9418, Adj. R^2 = 0.8379, Adeq. precision = 11.923.
A, temperature (°C); *B*, time (min); and *C*, gas ratio.

Table S4
Experimental CCD data for the BPA adsorption parameters using the as-synthesized CNMH

Sample ID	x_1 pH	x_2 dosage (mg)	x_3 contact time (min)	RV2 BPA removal (%)	Q adsorbent uptake (mg g^{-1})
B1	2.00	20.00	10.00	89.6677	112.081
B2	3.00	5.00	120.00	64.7360	323.680
B3	7.00	10.00	65.00	62.4294	156.074
B4	11.00	20.00	120.00	74.4173	93.022
B5	7.00	12.50	20.00	67.8316	135.663
B6	7.00	10.00	40.00	67.0425	167.606
B7	2.00	20.00	120.00	97.8012	122.251
B8	3.00	5.00	10.00	47.9074	239.537
B9	11.00	5.00	120.00	44.8118	224.059
B10	6.00	12.50	40.00	74.1442	148.288
B11	7.00	12.50	40.00	72.0501	144.100
B12	5.00	15.00	65.00	86.3141	143.857
B13	7.00	15.00	20.00	84.7056	141.176
B14	11.00	20.00	10.00	69.9256	87.407
B15	10.00	15.00	20.00	73.0971	121.829

Table S5
ANOVA results for BPA adsorption optimization to obtain the best BPA removal efficiency (RV2%) using the as-synthesized CNMH

Source	Sum of squares	df	Mean square	F Value	p Value Prob > F
Model	2,739.06	6	456.51	28.9	<0.0001
x_1	427.73	1	427.73	27.08	0.0008
x_2	1,260.95	1	1,260.95	79.82	<0.0001
x_3	197.71	1	197.71	12.52	0.0076
x_1x_2	240.372	1	240.372	15.44	0.0176
x_2x_3	43.84	1	43.84	2.78	0.1343
x_2^2	258.27	1	258.27	16.35	0.0037

R^2 = 0.9559, Adj. R^2 = 0.9228, Adeq. precision = 19.723.
x_1, pH; x_2, CNMH dosage (mg); and x_3, contact time (min).

Table S6
ANOVA results for BPA adsorption optimization to obtain the best adsorbent capacity (Q) using the as-synthesized CNMH

Source	Sum of squares	df	Mean square	F Value	p Value Prob > F
Model	53,404.52	9	5,933.84	93.42	<0.0001
x_1	1,429.52	1	1,429.52	22.51	0.0051
x_2	12,877.67	1	12,877.67	202.75	<0.0001
x_3	0.290	1	0.290	4.554×10^{-3}	0.9488
x_1x_2	1,380.95	1	1,380.95	21.74	0.0055
x_1x_3	318.70	1	318.70	5.02	0.0752
x_2x_3	1,639.68	1	1,639.68	25.82	0.0038
x_1^2	193.73	1	193.73	3.05	0.1412
x_3^2	69.11	1	69.11	1.09	0.3447
$x_1^2x_3$	281.62	1	281.62	4.43	0.0891

R^2 = 0.9941, Adj. R^2 = 0.9834, Adeq. precision = 36.048.
x_1, pH; x_2, CNMH dosage (mg); and x_3, contact time (min).